RESEARCH ARTICLE

NANO · MICRO small
www.small-journal.com

Development of ROS-Sensitive Sulfasalazine-Loaded Ferrocene Nanoparticles and Evaluation of Their Antirheumatic Effects in a 3D Synovial Hyperplasia Model

Dongwoo Kim, Chaehyun Kim, So Eun Lee, Sangwoo Kim, Sang-Il Lee, Min Hee Park, Mingyo Kim,* Daekyung Sung,* and Kangwon Lee**

Rheumatoid arthritis (RA) is a chronic inflammatory autoimmune disease characterized by joint inflammation, synovial hyperplasia, and bone and cartilage destruction, which significantly impairs physical function and quality of life. Disease-modifying antirheumatic drugs, such as sulfasalazine (SSZ), are crucial for altering the course and progression of RA; however, their clinical use is hampered by poor water solubility and lack of specificity for the reactive oxygen species (ROS)-rich environment typical of RA. To overcome these challenges, ROS-sensitive SSZ-loaded ferrocene nanoparticles are developed. The nanoparticles facilitate enhanced solubility and stability of SSZ and particularly enable precision targeting through the distinctive redox properties of ferrocene. Using a 3D synovial hyperplasia model with fibroblast-like synoviocytes derive from RA patients and validate at both the protein and gene levels, these nanoparticles significantly reduce lactate dehydrogenase, ROS, and inflammatory cytokine levels. Further validation using a collagen-induced arthritis model demonstrates therapeutic efficacy and cytokine modulation in vivo. These findings highlight the potential of ferrocene nanoparticles as a novel and effective therapeutic strategy for RA, offering improved drug delivery and reduced systemic toxicity.

1. Introduction

Rheumatoid arthritis (RA) is a chronic inflammatory autoimmune disorder characterized by persistent joint inflammation, synovial hyperplasia, and destruction of bone and cartilage. These conditions not only impair physical function and quality of life but also impose a significant socioeconomic burden.[1,2] Despite advances in understanding the pathophysiology of RA, effective and safe therapeutic interventions remain a pressing need in clinical practice. Disease-modifying antirheumatic drugs (DMARDs) are particularly noteworthy as they aim to alter the disease course, reduce or prevent joint damage, and improve long-term outcomes.[3,4] Commonly used conventional DMARDs include methotrexate, leflunomide, hydroxychloroquine, and sulfasalazine, each of which employs a distinct mechanism to modulate the immune response and inhibit RA progression.[5]

Among the DMARDs, sulfasalazine has been widely used in the management of RA because of its potent anti-inflammatory and immunomodulatory properties.[6] This drug is particularly effective in inhibiting the proliferation and activation of fibroblast-like synoviocytes (FLS) and immune cells such as macrophages, T cells, and B cells, all of which are crucial in the pathogenesis of RA. FLS plays a crucial role in sustaining inflammation and contributing to tissue destruction within the

D. Kim, C. Kim, K. Lee
Department of Applied Bioengineering
Graduate School of Convergence Science and Technology
Seoul National University
Seoul 08826, Republic of Korea
E-mail: kangwonlee@snu.ac.kr

C. Kim, S. Kim, D. Sung
Center for Bio-Healthcare Materials
Bio-Convergence Materials R&D Division
Korea Institute of Ceramic Engineering and Technology
Cheongju 28160, Republic of Korea
E-mail: dksung@kiset.re.kr

S. E. Lee, S.-I. Lee, M. Kim
Division of Rheumatology
Department of Internal Medicine
Gyeongsang National University Hospital
Jinju 52727, Republic of Korea
E-mail: mingyokim1@gnuh.co.kr

S. E. Lee, S.-I. Lee, M. Kim
Department of Convergence Medical Science
College of Medicine
Gyeongsang National University
Jinju 52727, Republic of Korea

The ORCID identification number(s) for the author(s) of this article can be found under https://doi.org/10.1002/smll.202407813

DOI: 10.1002/smll.202407813

joints.[7] They promote the production of inflammatory mediators and amplify inflammatory responses via interactions with immune cells, thereby exacerbating joint damage.[8,9] FLS are known to activate the nuclear factor kappa-light-chain-enhancer of activated B cells (NF-κB) signaling pathway, a key mediator of inflammation, which perpetuates the disease and worsens tissue damage.[10]

Sulfasalazine exerts its effects through multiple mechanisms, including inhibiting the NF-κB pathway, a key mediator of inflammation in FLS.[11] However, despite its clinical efficacy, sulfasalazine has several challenges that limit its utility as an optimal antirheumatic agent. However, a major limitation is its poor water solubility, which complicates its local delivery to inflamed joints.[12,13] This solubility issue hinders efficient drug concentration at target sites, reducing its therapeutic effectiveness. Additionally, sulfasalazine lacks specificity for the reactive oxygen species (ROS) prevalent in the inflamed synovium. This nonspecificity results in less targeted action within the rheumatoid synovial tissue, potentially affecting healthy tissues and causing off-target effects. Efforts to overcome these limitations have led to strategies such as structural modification of the drug, combination therapy with other DMARDs or biologics, and the development of novel delivery systems.[14,15] However, these approaches have not fully addressed the safety and efficacy concerns associated with sulfasalazine, underscoring the need for innovative solutions that enhance therapeutic specificity and reduce systemic toxicity.

Polymeric nanoparticles can achieve target specificity through passive targeting by focusing on macrophages that increase in inflamed joints. These nanoparticles can be efficiently phagocytosed by macrophages without surface modification, leveraging the fact that macrophages play a crucial role in rheumatoid arthritis. Nanoparticles are absorbed into the joints through macrophages via leaky capillaries in inflamed tissues, a process facilitated by the enhanced permeability and retention effect.[16,17] Stimulus-sensitive polymeric nanoparticles offer a promising solution for targeted drug delivery, particularly in environments with high ROS levels, such as inflamed tissues.[18] These nanoparticles are designed to respond to ROS levels that are ≈100 times higher (≈100 μM) in inflamed rheumatoid joints compared to normal tissues, enabling precise drug release at the target site.[19,20] Ferrocene, an organometallic compound with unique reversible redox activity and aqueous stability, is a key material for this purpose.[21] Upon oxidation, hydrophobic ferrocene (Fe^{2+}) transforms into hydrophilic ferrocenium (Fe^{3+}) without altering its molecular structure, thereby facilitating ROS-mediated drug release via a hydrophobic-to-hydrophilic transition.[22] However, owing to its hydrophobicity, ferrocene must be combined with hydrophilic blocks such as polyethylene glycol (PEG) to form amphiphilic polymers that impart colloidal stability, biocompatibility, and stealth properties to the nanoparticles.[23,24] These amphiphilic polymers can then form ROS-sensitive ferrocene nanoparticles in the shape of core–shell micelles.[25] These nanoparticles encapsulate hydrophobic drugs, such as sulfasalazine, in their core, enhancing solubility and bioavailability while reducing side effects.[26] Ferrocene-containing polymeric nanoparticles are particularly effective in the ROS-rich environment prevalent in the synovial tissues of patients with RA,[27] making them a versatile and effective component in the development of potent anti-inflammatory therapies for RA.

One significant hurdle in the development of effective antirheumatic drugs is the inability to accurately mimic RA in vitro. RA is particularly challenging in clinical settings because of the high heterogeneity among patients, which often forces clinicians to rely on their experience in selecting appropriate treatments.[28,29] This variability presents a significant hurdle in preclinical testing because accurately mimicking RA models is crucial for developing clinically applicable antirheumatic drugs. Our research group has previously succeeded in constructing a 3D synovial hyperplasia model using biocompatible polycaprolactone-micropatterned nanofibrous microwells based on FLS from five patients with RA.[30] In this study, we developed an RA 3D spheroid model that mimics the 3D environment of the human body, enabling high-throughput assays by culturing patient-derived synovial cells on a nanoscale-patterned polycaprolactone (PCL) scaffold. FLS from RA patients and human umbilical vein endothelial cells (HUVECs) were co-cultured to simulate vascular delivery. The constructed 3D spheroids were validated at the protein and gene levels and showed similarities to the synovial membranes of patients. The drug responsiveness to five DMARDs, including sulfasalazine, was evaluated by measuring changes in lactate dehydrogenase (LDH), ROS, and inflammatory cytokine levels.

In this study, we developed ROS-sensitive sulfasalazine-loaded ferrocene nanoparticles (SSZ@FcNPs) and tested their efficacy using a 3D synovial hyperplasia model constructed from FLS of patients with RA. This advanced 3D model, validated at both the protein and gene levels, closely mimicked the synovial environment found in patients with RA, providing a more accurate platform for drug testing. Our results demonstrated that SSZ@FcNPs effectively reduced LDH, ROS, and inflammatory cytokine levels, indicating significant anti-inflammatory and immunomodulatory effects. Additionally, we employed a collagen-induced arthritis (CIA) model to validate the therapeutic efficacy, cytokine modulation, and immune response of the nanoparticles. This study not only shows the potential of ferrocene polymers to enhance the solubility, stability, and target specificity of sulfasalazine but also underscores the innovative approach of using ROS-sensitive nanoparticles for targeted drug delivery. The successful application of these nanoparticles in both 3D synovial hyperplasia and CIA models underscores their potential as a more effective and safer therapeutic strategy for rheumatoid

S. Kim
Department of Chemical and Biomolecular Engineering
Yonsei University
50 Yonsei-ro, Seodaemun-gu, Seoul 03722, Republic of Korea
S.-I. Lee, M. Kim
Department of Internal Medicine
College of Medicine
Gyeongsang National University
Jinju 52727, Republic of Korea
M. H. Park
THEDONEE Inc.
Research Center
Seoul, South Korea
E-mail: minheepark@thedonee.com

arthritis, potentially overcoming the limitations of conventional treatments and improving patient outcomes.

2. Results and Discussion

2.1. Synthesis and Characterization of ROS-Sensitive FcPs for Targeted Drug Delivery

Ferrocene polymers represent a significant advancement in biomedicine, particularly in the development of drug delivery systems.[31,32] These polymers possess unique redox properties that allow their electrochemical behavior to be altered by changing their oxidation states through electron loss (oxidation) or gain (reduction). This reversible control of the redox processes makes ferrocene-containing copolymers highly effective for drug delivery applications, offering new avenues for targeted and controlled therapeutic interventions[25,33] (**Figure 1**).

We synthesized ROS-sensitive amphiphilic FcPs via straightforward radical polymerization using AIBN as the initiator. The polymer consisted of an FMMA monomer with a hydrophobic Fc moiety and MAA and PEGMA monomers with hydrophilic COOH and PEG groups. Five FcPs with different monomer ratios were synthesized via random radical copolymerization. The synthesized polymer was dissolved in DMSO-d_6 at 25 °C, and proton chemical shifts were recorded in parts per million (ppm) as follows: δ = h) 12.4 (br, 1H, COOH of MAA),[34] g) 4.8 (br, 2H, CO_2—CH_2 of FMMA), e,f) 4.4–4.1 (br, 9H of FMMA),[35] d) 3.77–3.61 (br, —OCH_2CH_2—, mPEGMA),[36] c) 3.38 (br, 3H, O—CH_3 of mPEGMA),[37] (solvent) 2.5 (DMSO-d_6),[36] a,b) 2.0–1.1 (br, —CH_3—, —CH_2—) (**Figure 2A**).[38]

To assess the purity of the synthesized FcPs, we analyzed the typical peaks of methacrylate protons of the FMMA, MAA, and PEGMA monomers, present between 5.38 and 6.21 ppm in the ^{1}H NMR spectrum.[39] Results indicated that all FcPs had conversion ratios above 99%, confirming a high polymer yield.[40] After polymerization, monomeric precursor peaks disappeared, replaced by broader peaks from polymeric alkyl chains (1.1–2.0 ppm). Molecular weight (Mw) and dispersity ($Đ_M = Mw/Mn$) of ferrocene-incorporating polymers were analyzed by GPC, calibrated with polystyrene (PS) standards. FcPs consistently exhibited PDI values below 2, indicating a relatively uniform molecular weight distribution, affirming successful polymerization (**Table 1**).

Critical micelle concentration (CMC) refers to the point at which amphiphilic polymers assemble into polymeric micelles when their concentration exceeds a specific threshold.[41] Determining the CMC value of amphiphilic polymers is critical for the formation of polymeric micelles.[42] Aqueous solutions of FcPs were analyzed across a concentration range from 5.05×10^{-8} to 4.04×10^{-6} mol L^{-1}. The scattering intensities measured at FcP concentrations below the CMC display a value that remains nearly steady. At the CMC, the intensity starts to increase linearly with concentration as the number of micelles in the solution grows. The CMC of FcPs was identified as 1.64×10^{-7} mol L^{-1} (Figure S1, Supporting Information).

FcNPs were easily prepared via nanoprecipitation of synthesized FcPs. These polymers can spontaneously form stable, self-assembled nanoaggregates in aqueous solutions with a hydrophobic ferrocene core and a hydrophilic shell comprising carboxyl and PEG groups. Nanoparticle stability is crucial for their biomedical applications.[43] To optimize them for further study, we compared FcNP stability under various conditions using DLS analysis. The initial assessment involved measuring hydrodynamic diameter and PDI in DI water (25 °C) on the day of fabrication. While the PDI of FcNP1 was <0.2, its hydrodynamic diameter showed some microscale aggregation. Random copolymers of FMMA and MAA alone displayed instability; however, the addition of PEGMA significantly improved the nanoparticle stability (Figure 2B).[44] Therefore, only FcNP2s through FcNP5s were evaluated for long-term stability. All particles, except FcNP2s, which aggregated on day 7, remained stable in aqueous solution for 42 days, with minimal changes in hydrodynamic diameter and PDI. This was likely due to slightly lower PEG content reducing stabilization and causing precipitation (Figure 2C).[45] Notably, FcNP3s, FcNP4s, and FcNP5s maintained stability even after lyophilization and redispersion without cryoprotectants (Figure 2D). Lyophilization, which involves the removal of water through sublimation, is typically recommended to prevent physicochemical and microbiological issues.[46] This finding highlights the exceptional stability of the FcNPs under diverse conditions, making them promising candidates for drug delivery platforms.

Micelles made from polymers with stealth properties, such as PEG, extend the circulation time in blood.[47] Upon reaching diseased areas with high local ROS concentrations, micelles disintegrate and release the encapsulated drugs.[25] We assessed ROS sensitivity by exposing FcNPs to 100 mM H_2O_2 and measuring the changes in the hydrodynamic diameter. The increase in diameter after exposure depended on the exposure duration, with FcNP3s showing the quickest response, followed by FcNP4s and FcNP5s (Figure 2E). This suggests that a higher PEG density on micelle surfaces enhances particle stability,[48] reducing ROS sensitivity of hydrophobic ferrocene domains and prolonging reaction and degradation times. Zeta potential measurements confirmed the ROS sensitivity of FcNP3s through an increased surface charge upon oxidation.[49] TEM images before and after oxidation validated the morphological changes, demonstrating the potential of FcNP3s as smart ROS-sensitive carriers for efficient drug delivery (Figure 2F).

2.2. Optimization and Characterization of FcNPs for Targeted SSZ Delivery

Stimuli-sensitive polymers play a crucial role in biomedical applications where precise drug delivery is essential to avoid toxicity and ensure efficacy.[26] FcNPs have been engineered to release their therapeutic payload in response to ROS, facilitating the targeted delivery of SSZ for sustained treatment of rheumatoid arthritis (RA) (**Figure 3A**).

Various amounts of SSZ were loaded into FcNP3s to create SSZ@FcNPs, which were visualized in photographic images (Figure S2, Supporting Information). The encapsulation of SSZ did not significantly alter the physicochemical properties (hydrodynamic diameter and PDI) of FcNP3s until the SSZ content reached 20 wt.%. Zeta potential measurements indicated that SSZ@FcNPs with 5 and 10 wt.% SSZ showed no

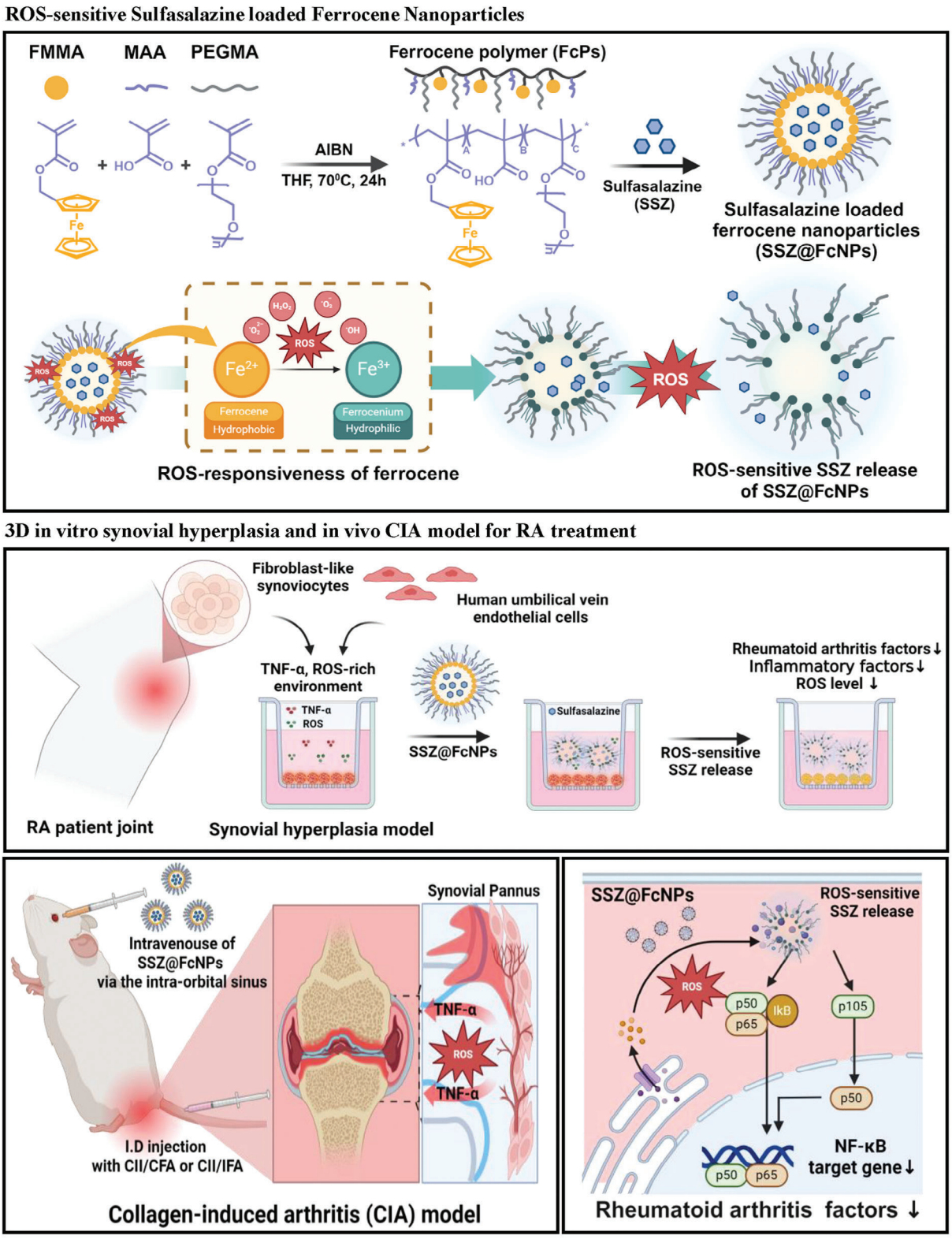

Figure 1. Schematic illustration of the development of ROS-sensitive sulfasalazine loaded ferrocene nanoparticles and antirheumatic drug evaluation in 3D synovial hyperplasia model.

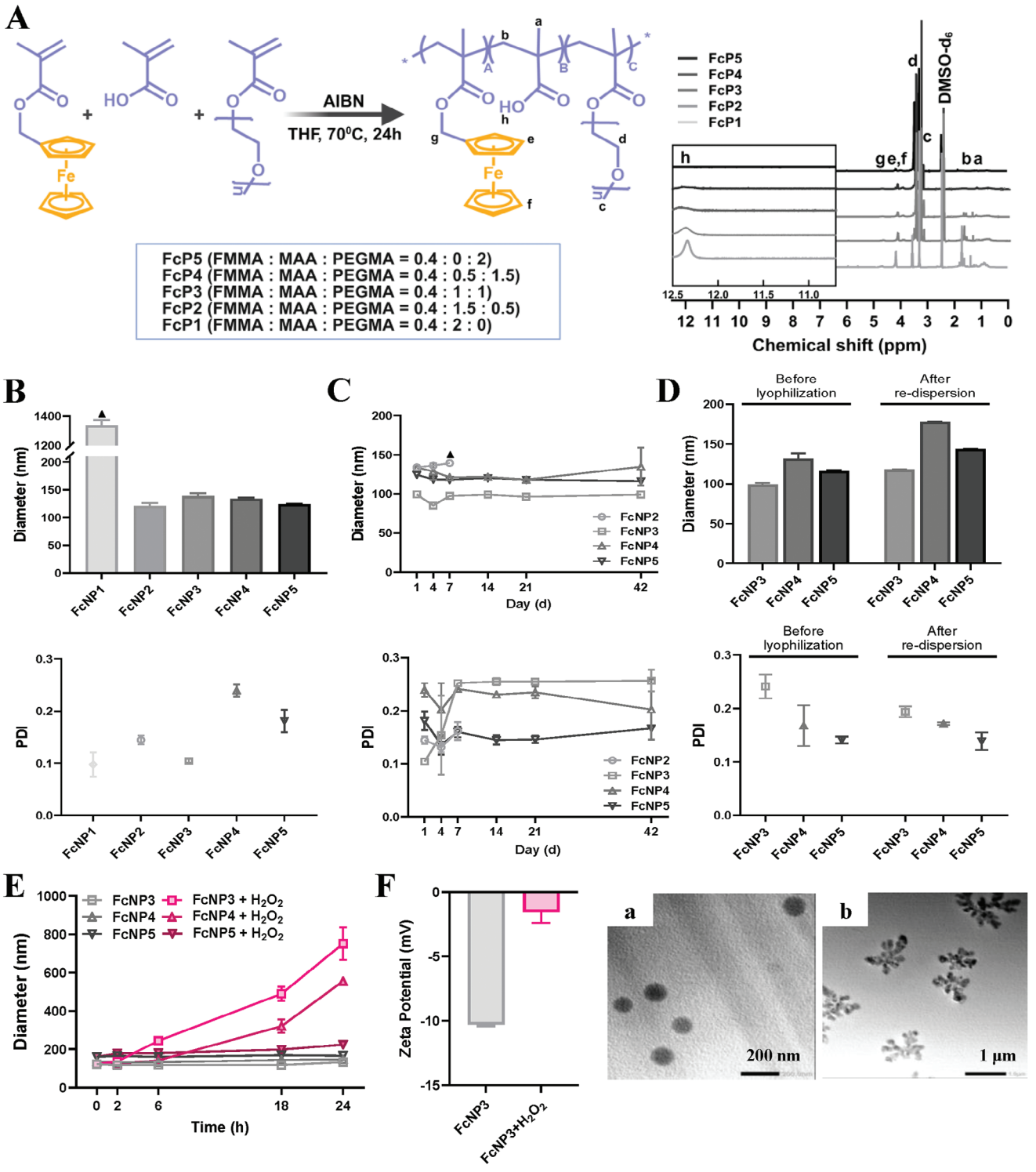

Figure 2. Synthesis and analysis of ferrocene polymers and nanoparticle properties. A) Synthetic pathway of ferrocene polymers formulated by varying the molar ratios of the monomers. Proton nuclear magnetic resonance (^{1}H NMR) spectra of ferrocene polymers in DMSO- d_6 with chemical structure and peak assignments. Hydrodynamic diameter and PDI of B) Initial FcNP1-5s, C) FcNP2-5s for 42 days. The symbol (▲) denotes partial aggregation of the nanoparticles, and D) FcNP3-5s before lyophilization and after re-dispersed in DIW without any cryoprotectants (n = 3). E) The variations of ROS-sensitive hydrodynamic diameter of FcNP3-5s (n = 3). F) Zeta potential (n = 3), and TEM images of FNP3s a) before (Scale bar: 200 nm) and b) after (Scale bar: 1 μm) treatment of 100 mM H_2O_2 in DIW for 24 h.

Table 1. Analysis of the synthesized ferrocene polymers along with the number-average molecular weight (M_n), the weight-average molecular weight (M_w), and dispersity ($Đ_M$) of the copolymers synthesized with different monomer contents (mol%).

Physicochemical analysis of the synthesized ferrocene polymers by NMR and GPC

Polymer	Monomer feed [mol%]			Polymer feed [mol%]			Conversion[a)] [%]	M_n[b)] [g mol^{-1}]	M_w[b)] [g mol^{-1}]	$Đ_M$[b)]
	FMMA	MAA	PEGMA	FMMA	MAA	PEGMA				
FcP1	16.7	83.3	0	22.05	77.95	0	99.34	2985	5601	1.876
FcP2	16.7	62.5	20.8	21.33	57.76	20.9	99.78	6806	12928	1.899
FcP3	16.7	41.7	41.7	18.54	37.82	43.64	99.98	7048	12368	1.755
FcP4	16.7	20.8	62.5	17.65	20.3	62.06	99.96	7421	12803	1.725
FcP5	16.7	0.0	83.3	18.2	0	81.8	99.8	6822	12013	1.761

[a)] Measured by ^{1}H NMR spectroscopy; [b)] Measured by GPC via relative calibration curve with polystyrene standards.

significant change compared to SSZ@FcNPs without SSZ, suggesting SSZ primarily localized in the core. However, at the concentration of 20 wt.%, the zeta potential was lower than that of SSZ@FcNPs without SSZ, indicating that the nanoparticles had reached saturation and became unstable. The negatively charged sulfasalazine influenced the zeta potential of 20 wt.% particles, resulting in a more negative charge compared to other particles (Figure 3B).[50]

The HPLC analysis results at the 20 wt.% also support this saturation state. The loading content (L.C.) and encapsulation efficiency (E.E.) were determined using HPLC analysis for different SSZ contents: 5 wt.% SSZ@FcNPs: L.C. = 4.86, E.E. = 97.29; 10 wt.% SSZ@FcNPs: L.C. = 9.76, E.E. = 97.62; 20 wt.% SSZ@FcNPs: L.C. = 18.39, E.E. = 91.95. The E.E. at 20 wt.% is ≈6% lower than at 5 and 10 wt.%. This indicates a greater loss due to saturation. Owing to this saturation, a slight increase in the particle size was observed, and the precipitation of some unstable polymer particles was observed on the third day after particle fabrication (Figure S3, Supporting Information). Therefore, 20 wt.% concentration was completely excluded from the optimization process.

The physicochemical properties (hydrodynamic diameter and PDI) of SSZ@FcNPs (5 and 10 wt.%) were evaluated over 84 days to demonstrate their long-term stability in aqueous solutions (Figure 3C). The results confirmed high stability up to a concentration of 10 wt.%, leading to the selection of SSZ@FcNP 10 wt.% (0.1 mg ml^{-1}) as the optimal formulation for further studies.

To assess the ROS-sensitive properties of SSZ@FcNPs, changes in hydrodynamic diameter and cumulative SSZ release were monitored in the presence and absence of 100 µM H_2O_2 in phosphate-buffered saline (PBS) (37 °C, 100 rpm).[51] Before oxidation, SSZ release from SSZ@FcNPs was minimal because of the stability of the nanoparticles. In contrast, exposure to 100 µM H_2O_2 induced rapid swelling of SSZ@FcNPs, resulting in burst release of SSZ. This swelling was attributed to the electrostatic repulsion between ferrocenium ions (Fe^{3+}) generated in the oxidized ferrocene core, leading to the rapid release of encapsulated SSZ from the hydrophobic core (Figure 3D).[49,52,53]

The ROS sensitivity of SSZ@FcNPs was further confirmed using photographic and TEM images, illustrating the expansion of FcNPs in response to ROS, which created larger diffusion spaces (Figure 3D).

2.3. Stability Evaluation of Enriched SSZ@FcNPs for Enhanced In Vivo SSZ Delivery

Previous in vivo studies in mouse models have utilized ferric ions and SSZ-loaded nanoparticles for anti-inflammatory treatments at high SSZ doses, typically ≈50 mg kg^{-1}.[54] Given that DBA/1J mice used in our current experiment have an average body weight of ≈20 g,[55] the optimized SSZ@FcNPs (0.1 mg mL^{-1}) prepared earlier necessitate a high dosage. Hence, we developed enriched SSZ@FcNPs.

Initially, we assessed the hydrodynamic diameters and PDI of 4× and 8× enriched FcNPs to determine the optimal enrichment level, ensuring the stable formation of FcNPs. By Day 14 of FcNP production, the hydrodynamic diameter, and PDI of 8× enriched FcNPs had significantly increased (Figure S4, Supporting Information). Consequently, 4× enriched FcNPs were loaded with a 4× SSZ amount to prepare 4× enriched SSZ@FcNPs (0.4 mg mL^{-1}). Evaluation of hydrodynamic diameter and PDI changes in 4× enriched FcNPs and SSZ@FcNPs under PBS conditions at 37 °C over 14 days revealed that 4× enriched SSZ@FcNPs exhibited excellent stability (Figure S5, Supporting Information). Furthermore, the particle morphology of the 4× enriched SSZ@FcNPs was confirmed using TEM (Figure S6, Supporting Information).

2.4. Effectiveness of SSZ@FcNPs on In Vitro 3D Synovial Hyperplasia Model

Traditional 2D flask-based in vitro tests often fail to accurately reflect complex cellular interactions and tissue environments encountered in clinical settings, particularly in diseases such as RA.[56,57] To address these limitations, we developed a 3D in vitro synovial hyperplasia model that incorporates key features of RA pathology,[30] such as neo-vascularization,[58] cell-extracellular matrix interactions,[59] and an inflammatory milieu[60] using HUVECs, PCL nanofibers, and TNF-α activation.

In this study, we evaluated the antirheumatic effects of SSZ@FcNPs using our established 3D hyperplasia model. FLSs and HUVECs were seeded into nanofibrous microwells and allowed to reconstruct over four days. Following activation with TNF-α to induce an inflammatory response in FLSs, drug treatments were administered (**Figure** 4A). A quantitative assessment

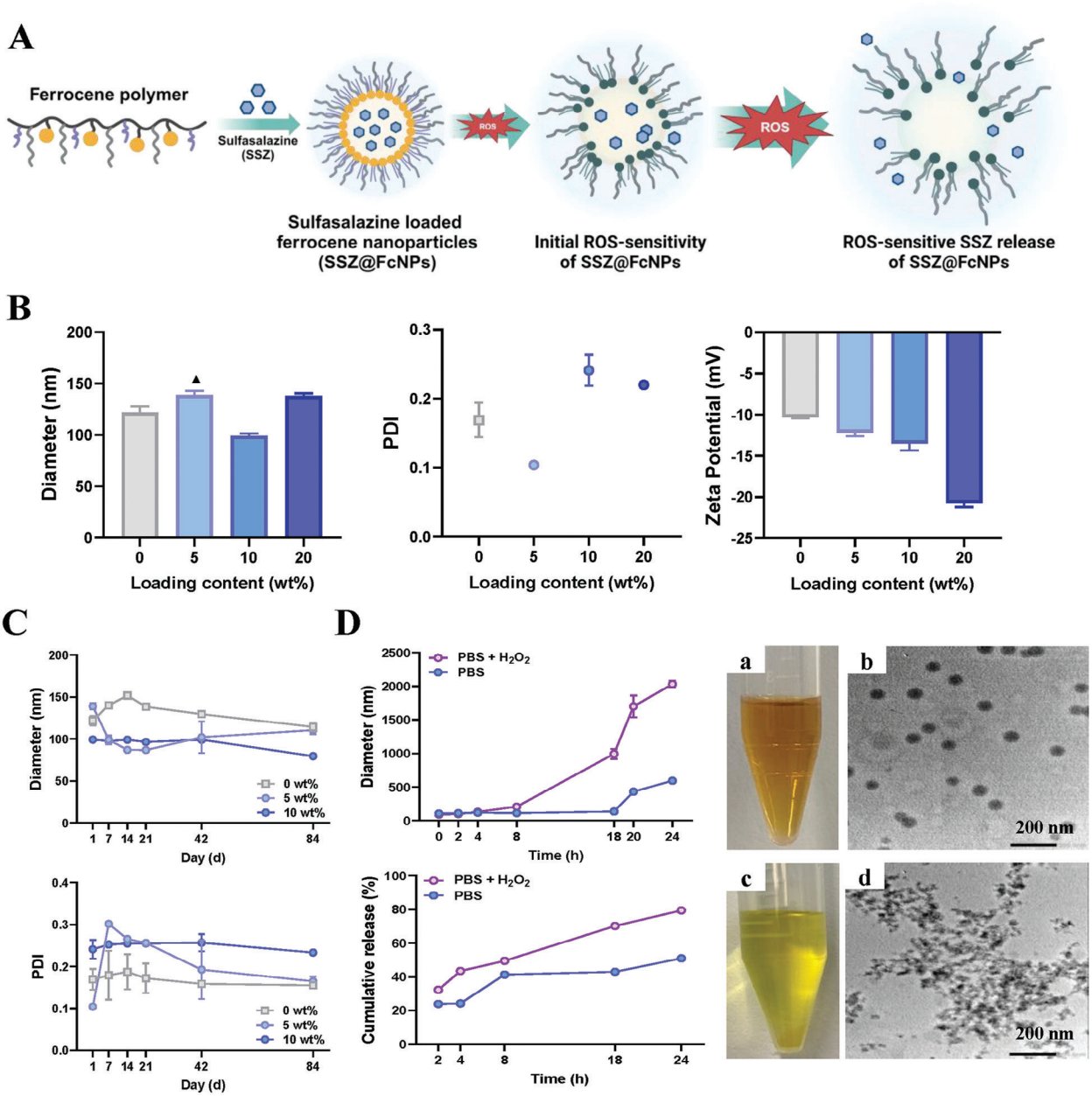

Figure 3. Fabrication, ROS-responsive properties, and stability analysis of Sulfasalazine-loaded ferrocene nanoparticles. A) Schematic illustration of fabrication and ROS-sensitive properties of Sulfasalazine loaded ferrocene nanoparticles. B) Initial hydrodynamic diameters, PDI, and zeta potential of SSZ@FcNPs with loading contents ranging from 0 to 20 wt.% ($n = 3$). C) Long-term stability analysis of SSZ@FcNPs (0, 5, and 10 wt.%) for 84 days in DIW ($n = 3$). D) ROS-sensitive properties of SSZ@FcNPs. The variations of hydrodynamic diameter and cumulative SSZ release of SSZ@FcNPs after treating 100 μM H_2O_2 in PBS ($n = 3$), and photograph and TEM images (Scale bar: 200 nm) of SSZ@FcNPs [a,b) Before oxidation in PBS, c,d) After oxidation in PBS for 24 h].

of cell damage induced by drug treatments at various concentrations was conducted using an LDH assay (Figure 4B). Notably, the SSZ@FcNP group exhibited significantly enhanced cell damage compared to free SSZ, suggesting that SSZ@FcNPs enhance drug efficacy, likely due to the hydrophobic-to-hydrophilic transition of FcNPs upon oxidation,[32] enabling controlled and localized SSZ release.

To further evaluate the efficacy of SSZ@FcNPs in mitigating oxidative stress, a DCFDA/H2DCFDA assay was performed to measure ROS levels produced by FLSs (Figure 4C). The significant reduction in ROS levels observed in the SSZ@FcNP group compared to those in the free SSZ underscores the effectiveness of FcNPs in ROS-rich environments, consistent with their known properties.[18]

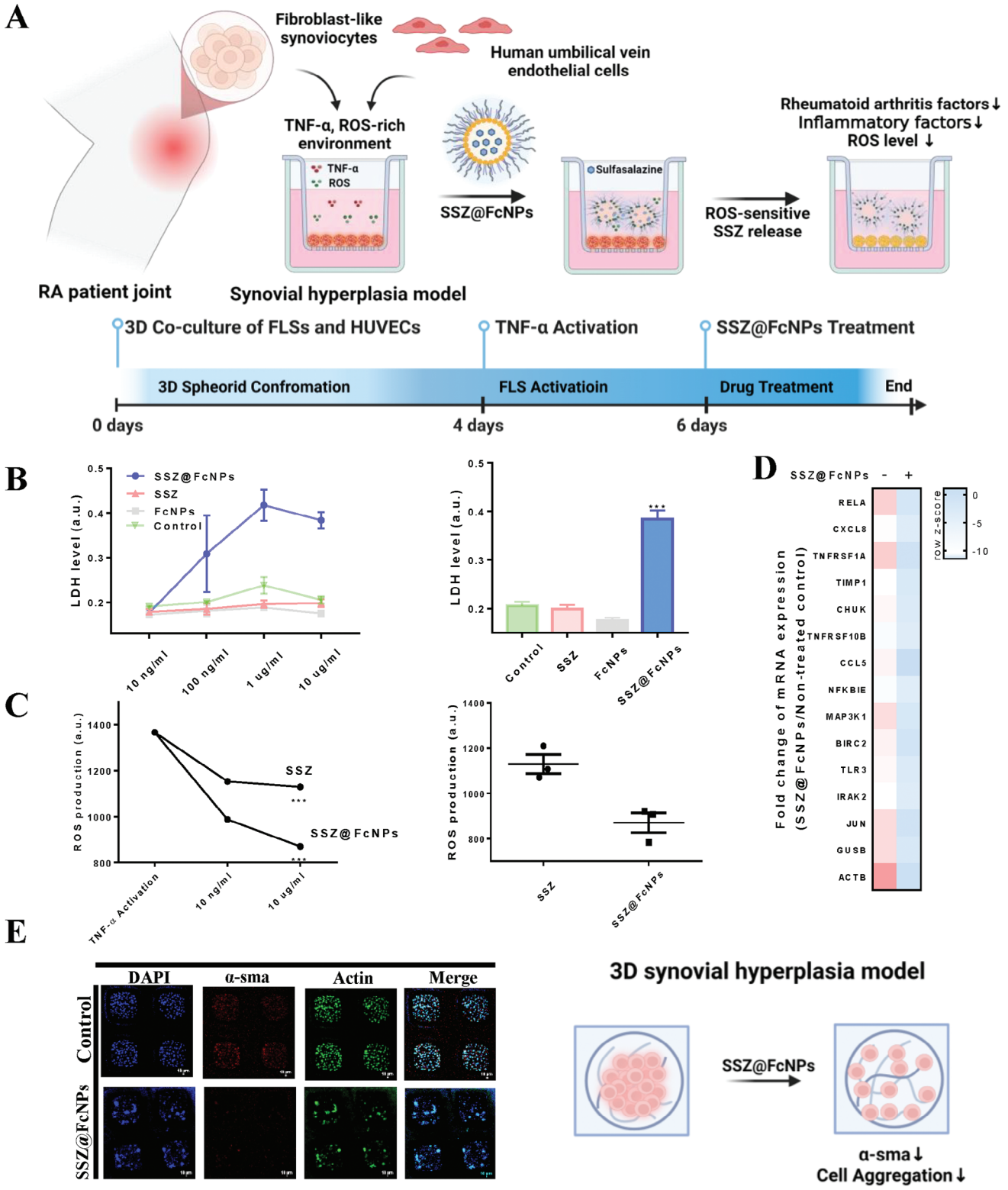

Figure 4. Evaluation of antirheumatic effects of SSZ@FcNPs in a 3D in vitro synovial hyperplasia model. A) Schematic illustration of the 3D in vitro synovial hyperplasia model used to test the antirheumatic effect of SSZ@FcNPs. B) Changes in LDH levels after treatment with varying concentrations of control (media only), SSZ, FcNPs, and SSZ@FcNPs ($n = 3$). C) Measurement of ROS levels following treatment with SSZ@FcNPs ($n = 3$). D) Gene expression changes following treatment with SSZ@FcNPs. E) Fluorescent images showing cell migration and cell–cell adhesion expression following treatment with SSZ@FcNPs in the 3D in vitro synovial hyperplasia model (Scale bar: 10 μm). Values are the mean ± SEM; ***$p < 0.001$ versus the control group.

Gene expression changes in inflammatory markers were assessed using qRT-PCR before and after SSZ@FcNP treatment to evaluate the drug-induced effects on FLSs and changes in ROS levels (Figure 4D). Downregulation of key inflammatory markers such as CCL5[61] and TNFRSF1A[62] demonstrated that FcNPs facilitated cellular uptake and sustained SSZ release, leading to effective suppression of inflammatory factors at the molecular level.

Qualitative assessment of the impact of SSZ@FcNPs on the 3D spheroid model included α-SMA staining for cell migration and 4',6-diamidino-2-phenylindole (DAPI) staining for cell aggregation (Figure 4E). Treatment with SSZ@FcNPs resulted in reduced α-SMA expression and decreased cell aggregation, further supporting the therapeutic benefits of SSZ@FcNPs in inhibiting cell migration and synovial hyperplasia.[63]

In summary, the application of SSZ@FcNPs to our 3D synovial hyperplasia model derived from RA patient cells demonstrated concentration-dependent cell damage, reduced ROS levels, downregulation of inflammation-related genes, and decreased cell migration and aggregation. These findings highlight the potential of NP-based drug delivery systems in enhancing drug efficacy, minimizing side effects, and providing sustained therapeutic benefits in the treatment of rheumatoid arthritis.

2.5. Enhanced Inhibition of NF-κB Signaling Pathway in Rheumatoid Arthritis through SSZ@FcNPs

SSZ is a well-known DMARD that inhibits the NF-κB signaling pathway, thereby reducing inflammatory cytokine levels and mitigating the severity of RA.[64,65] This study investigated the effectiveness of SSZ@FcNPs, developed to enhance SSZ delivery and efficacy via ferrocene nanoparticle encapsulation, in inhibiting the NF-κB pathway (**Figure 5A**).

First, a western blot assay was conducted to assess NF-κB pathway inhibition at the protein level (Figure 5B). Following TNF-α treatment to induce inflammation, the control group showed increased expression of all proteins tested. Compared to free SSZ, the SSZ@FcNPs exhibited a significant reduction in NF-IκB, NF-κB p65, NF-κB p105, and NF-κB p50 levels, indicating superior inhibition of the NF-κB pathway. This enhanced efficacy is attributed to the responsive nature of FcNPs, which undergo a hydrophobic-to-hydrophilic transition upon oxidation in ROS-rich synovial tissues.[66] This transformation facilitates targeted and controlled SSZ release, ensuring higher drug concentrations at inflamed sites and thereby more effectively inhibiting NF-κB signaling and subsequent inflammatory cytokine production.

Subsequently, a dot blot assay was employed to quantify the inhibition of inflammatory cytokines downstream of NF-κB inhibition (Figure 5C). Significant reductions were observed in multiple inflammatory cytokines, notably IL-1β, IL-3, IL-4, IL-6sR, IL-12 p40, and p70,[67] further validating the potent anti-inflammatory effects of SSZ@FcNPs. By broadly inhibiting cytokines crucial to RA pathogenesis, SSZ@FcNPs not only target primary inflammatory signals but also modulate downstream effects, providing comprehensive anti-inflammatory action.

To evaluate the impact of SSZ@FcNPs on macrophages, their response was examined for M1 polarization, a marker of pro-inflammatory activation. Immunofluorescence staining revealed no induction of M1 polarization in macrophages treated with SSZ@FcNPs, similar to controls, in contrast to the positive control lipopolysaccharide (LPS) (Figure 5D). This demonstrates the specificity of SSZ@FcNPs in targeting FLSs without triggering pro-inflammatory responses in macrophages, which is crucial for avoiding additional inflammation and tissue damage.[68]

Furthermore, western blot analysis of IL-1β protein levels confirmed that SSZ@FcNPs did not induce inflammatory responses in macrophages (Figure 5E), ensuring their biocompatibility and safety profile. This finding indicated that SSZ@FcNPs selectively target FLSs, reduce disease severity, and do not elicit inflammatory or immune responses in other cell types, thereby positioning them as a safe therapeutic option for RA treatment.[69]

In conclusion, SSZ@FcNPs effectively inhibit the NF-κB signaling pathway compared to free SSZ, leading to reduced inflammatory cytokine production. Their ability to suppress inflammation without inducing immune responses in macrophages highlights the dual benefits of enhanced efficacy and safety, making SSZ@FcNPs a promising therapeutic approach for the treatment of rheumatoid arthritis.

2.6. SSZ@FcNPs Effects in Collagen-Induced Arthritis (CIA) Mouse Model

SSZ has shown efficacy in inhibiting the proliferation and activation of key cells involved in RA, such as FLS, macrophages, T cells, and B cells, primarily through the NF-κB pathway.[64,70,71] However, its limitations include poor water solubility, hindering its effective local delivery to inflamed joints, and a lack of specificity for the ROS-rich environment typical of inflamed synovium.[12,13] To overcome these challenges, hydrophobic drugs like sulfasalazine were encapsulated in nanoparticles to enhance solubility and bioavailability.[26] Our in vitro studies demonstrated that SSZ@FcNPs regulate the NF-κB pathway, leading to suppression of ROS generation and reduction in inflammatory cytokine production, suggesting promising therapeutic benefits for RA.

To further investigate this potential, we evaluated the therapeutic efficacy of SSZ@FcNPs using a collagen-induced arthritis (CIA) mouse model that mimics the key pathological features of RA. Mice were immunized with bovine type II collagen/complete Freund's adjuvant (CII/CFA) on day 0 and boosted with bovine type II collagen/incomplete Freund's adjuvant (CII/IFA) on day 21 to induce CIA. Subsequently, mice were intravenously administered PBS, SSZ, FcNPs, or SSZ@FcNPs via the intra-orbital sinus starting on day 1, with subsequent administrations twice weekly (**Figure 6A**). Notably, none of the treatment groups exhibited significant weight loss (Figure S7, Supporting Information).

Histopathological analysis of kidney, liver, and spleen tissues using hematoxylin and eosin (H&E) staining showed no signs of toxicity with FcNPs and SSZ@FcNPs compared to PBS and SSZ, corroborated by serum levels of urea and creatinine (Figures S8,S9, Supporting Information). These results confirmed the safety of the nanoparticles developed in this study in terms of systemic toxicity.

The assessment of arthritis severity using clinical scores revealed that neither SSZ nor FcNP monotherapy significantly

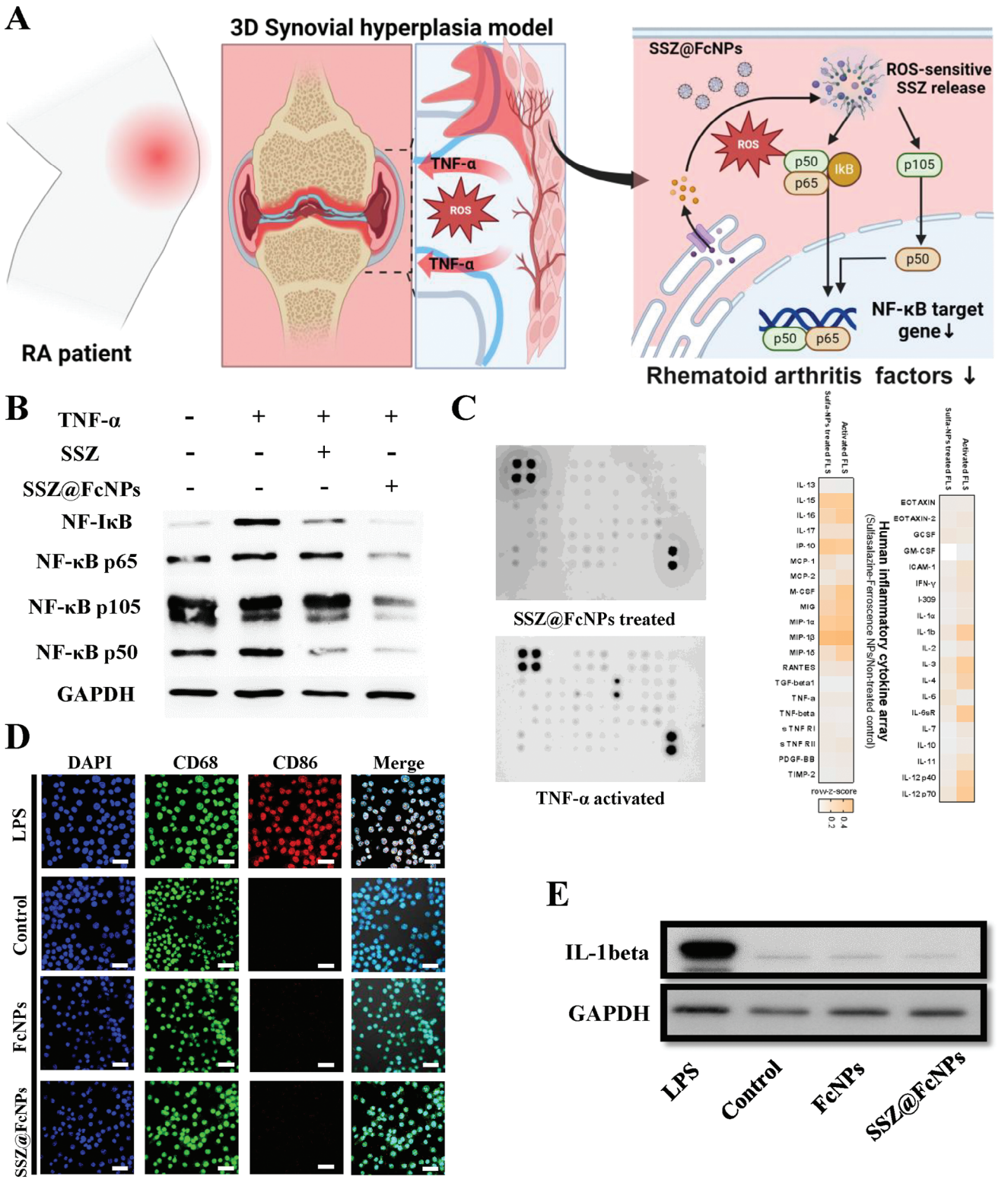

Figure 5. Inhibition of NF-κB signaling and inflammatory response by SSZ@FcNPs in a patient cell-based 3D microenvironment. A) Schematic illustration of the patient cell-based 3D microenvironment and the inhibitory effect of SSZ@FcNPs on the NF-κB signaling pathway. B) Western blot image showing the inhibitory effect of SSZ@FcNPs on the NF-κB signaling pathway in the patient cell-based 3D microenvironment. C) Dot blot assay of inflammatory cytokines in response to FcNPs and SSZ@FcNPs. D) Fluorescent image of macrophage polarization induced by SSZ@FcNPs (Scale bar: 20 μm). E) Western blot of the inflammatory response to FcNPs and SSZ@FcNPs nanoparticles in RAW264.7 cells.

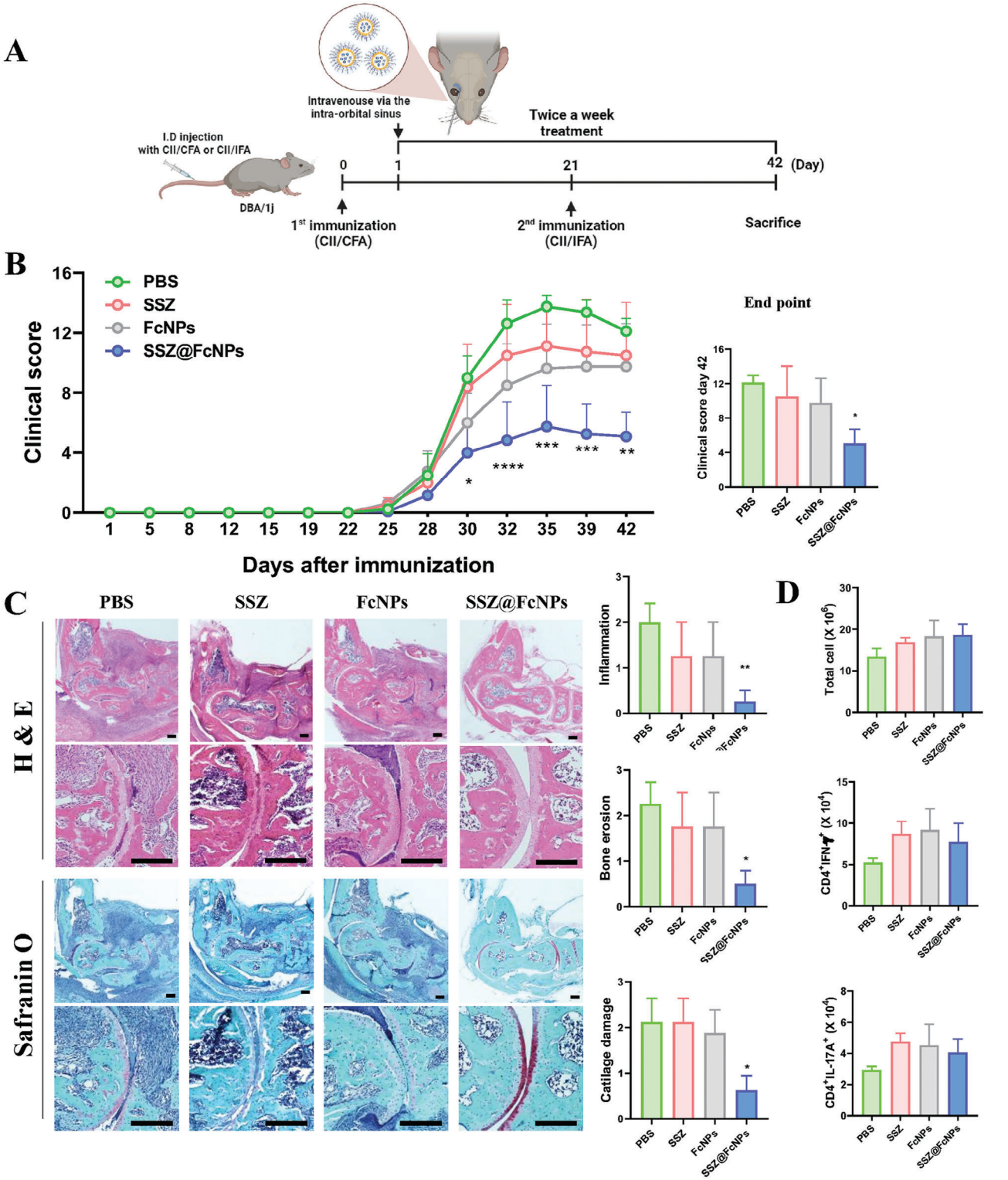

Figure 6. Therapeutic efficacy of SSZ@FcNPs in CIA mice: clinical scores, histopathology, and severity of joint inflammation and damage. A) Timetable of a therapeutic regimen with a CIA induction. Mice were immunized with bovine type II collagen on days 0 and 21. During the induction of CIA, the mice were administered PBS ($n = 4$), SSZ ($n = 4$), FcNPs ($n = 4$), or SSZ@FcNPs ($n = 5$) twice a week starting from day 1 until the day of sacrifice (day 42). B) Changes in clinical score were observed during the 42 days after CIA induction. C) Representative histopathological images and scores of ankle joints stained with H&E and safranin O. (original magnification × 20, 100). The severity scores of inflammations, bone erosions, and cartilage damage in ankle joints are graded on a scale ranging from 0 (none) to 3 (severe). Scale bar: 200 μm Values are the mean ± SEM ($n = 4$–6 mice for each group); *$p < 0.05$; **$p < 0.01$; ***$p < 0.001$; ****$p < 0.0001$ versus PBS-treated CIA mice.

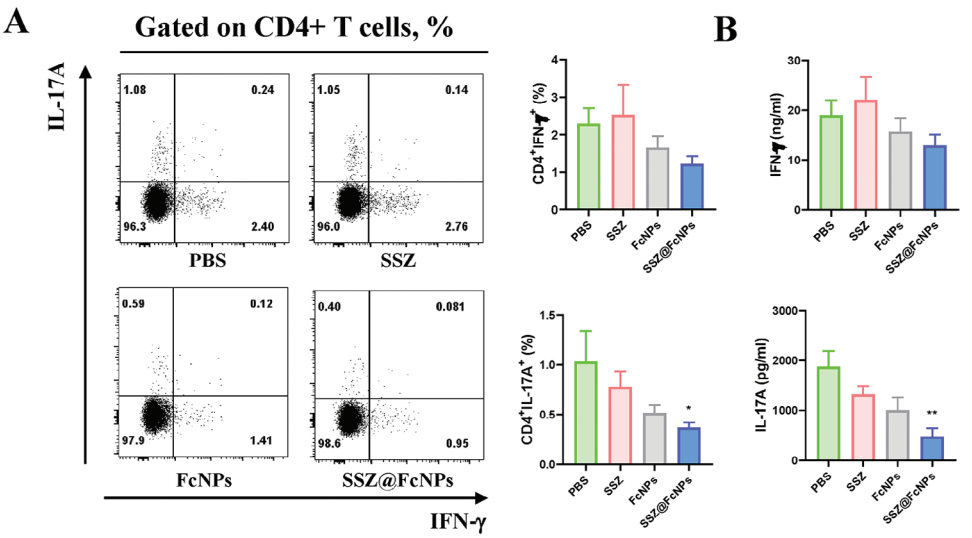

Figure 7. Analysis of IFN-γ and IL-17A production in CD4$^+$ T cells from iLN of treated CIA mice by flow cytometry and ELISA. A) The frequency of IFN-γ and IL-17A-producing CD4$^+$T cells in the iLN from PBS, SSZ, FcNPs, and SSZ@FcNPs-treated mice at 42 days after immunization were analyzed by flow cytometry. B) iLN cells were collected from mice at 42 days after CIA induction, and 2 × 10^5 iLN cells stimulated with anti-CD3 and anti-CD28 antibodies for 48 h. Levels of IFN- γ and IL-17A in culture supernatants were measured by ELISA. Values are the mean ± SEM (n = 4– mice for each group); *p < 0.05; **p < 0.01 versus PBS-treated CIA mice.

reduced arthritis severity in the CIA model. In contrast, mice treated with SSZ@FcNPs showed significantly lower mean arthritic clinical scores compared to PBS-, SSZ-, or FcNPs-treated mice (Figure 6B).

Further evaluation through histopathological examination using H&E and safranin O staining demonstrated a marked reduction in joint inflammation, bone erosion, and cartilage damage in SSZ@FcNPs-treated CIA mice compared to the controls (Figure 6C). These findings underscore the efficacy of SSZ@FcNPs in preventing arthritis development in the CIA model, which is attributed to its targeted specificity for rheumatoid arthritis and ROS sensitivity.

In summary, SSZ@FcNPs effectively attenuated the severity of arthritis in the CIA mouse model by targeting inflammation and protecting joint integrity. This study highlights the potential of SSZ@FcNPs as a promising therapeutic strategy for rheumatoid arthritis, offering enhanced efficacy and safety profiles compared to conventional SSZ treatment approaches.

2.7. Immune Modulation of SSZ@FcNPs during CIA Development

Th17 cells play a crucial role in the pathogenesis of autoimmune arthritis,[72–74] particularly through the secretion of IL-17A, a pro-inflammatory cytokine known to exacerbate arthritic symptoms in CIA models.[75] To assess the immunological effects of SSZ@FcNPs, we conducted flow cytometry analysis on inguinal lymph nodes isolated from CIA mice on day 42 post-immunization.

Flow cytometry analysis revealed a significant reduction in the percentage of Th17 cells (CD4$^+$IL-17A$^+$) in SSZ@FcNPs-treated CIA mice compared to that in the PBS-, SSZ-, and FcNPs-treated groups. Notably, there was no significant difference in the frequency of Th1 cells (CD4$^+$IFN-γ^+) between SSZ@FcNPs-treated mice and the control groups (**Figure** 7A). Consistent with the percentage results from flow cytometry, cell count analysis of the inguinal lymph nodes showed a significant decrease in Th17 cell (CD4$^+$IL-17A$^+$) counts in SSZ@FcNPs-treated CIA mice compared to the PBS-, SSZ-, and FcNPs-treated groups. A decreasing trend in Th1 cell (CD4$^+$IFN-γ^+) counts was also observed in SSZ@FcNPs-treated CIA mice compared to the control groups, but this was not statistically significant. Additionally, no differences in the total cell counts were observed among the groups (Figure S10, Supporting Information).

To further explore the impact of SSZ@FcNPs on T-cell cytokine production, inguinal lymph node cells from CIA mice were isolated and stimulated with anti-CD3/CD28 antibodies for 48 h. Supernatants were collected and analyzed for cytokine production using ELISA. Consistent with the flow cytometry results, SSZ@FcNPs treatment significantly reduced IL-17A production in response to CD3/CD28 stimulation compared to PBS, SSZ, and FcNPs treatments. However, there was no significant difference in IFN-γ production among the groups (Figure 7B).

The observation that SSZ@FcNPs treatment specifically suppressed IL-17A production without affecting IFN-γ suggests a selective modulation of Th17 cells, key mediators in autoimmune arthritis. These findings support the hypothesis that SSZ@FcNPs mitigate CIA pathology by targeting Th17 cells and reducing IL-17A production, thereby contributing to the amelioration of arthritis symptoms.

In conclusion, SSZ@FcNPs exhibit immunomodulatory effects in the CIA mouse model by specifically targeting Th17 cells and suppressing IL-17A production. This selective modulation highlights the potential therapeutic utility of SSZ@FcNPs in autoimmune arthritis, providing a targeted approach to alleviate disease severity without affecting other immune responses such as Th1 cell activity.

3. Conclusion

In summary, we successfully demonstrated the synthesis, characterization, and application of ROS-sensitive ferrocene nanoparticles (FcNPs) for targeted drug delivery, specifically focusing on sulfasalazine (SSZ) delivery. The unique redox properties of ferrocenes allowed for the alteration of polymer behaviors, enabling effective controlled drug release mechanisms. In vitro studies utilizing a 3D synovial hyperplasia model, which mimics rheumatoid arthritis (RA) conditions, demonstrated that SSZ@FcNPs effectively reduced ROS levels, downregulated inflammation-related genes, and mitigated cell migration and aggregation. Moreover, in vivo studies using a CIA mouse model corroborated the therapeutic benefits of SSZ@FcNPs. Treatment with SSZ@FcNPs significantly reduced arthritis severity, joint inflammation, bone erosion, and cartilage damage compared to control groups. Furthermore, immune modulation studies revealed a notable reduction in IL-17A production by Th17 cells, indicating the immunomodulatory effects of SSZ@FcNPs. This study provides a solid foundation for further optimizing and developing ferrocene-based drug delivery systems across a broad spectrum of biomedical applications.

4. Experimental Section

Synthesis of Ferrocene Polymers (FcPs): Radical polymerization was employed to synthesize ferrocene polymers (Poly (FMMA-*r*-MAA-*r*-PEGMA)). Before initiating the polymerization, MAA and PEGMA were passed over a column containing an inhibitor removal system for 1 and 3 h, respectively. To synthesize the copolymers, Ferrocenylmethyl methacrylate (FMMA, 95%), methacrylic acid (MAA, 99%), and poly (ethylene glycol) methyl ether methacrylate (PEGMA, 99%; Mn = 500 g mol^{-1}) were dissolved in 10 mL of tetrahydrofuran (THF, anhydrous, 99.9%). The inhibitor-removal columns, FMMA, MAA, PEGMA, and THF, were obtained from Sigma-Aldrich (St. Louis, MO, USA). The molarity of FMMA was set to 0.4 mmol, and the ratios of MAA to PEGMA were adjusted from 2 to 0 mmol and from 0 to 2 mmol, respectively, creating a library with different proportions of five species. Next, 0.12 mmol of 2,2-Azobisisobutyronitrile (AIBN, 99%) (Daejung, Seoul, Korea) was added as a radical initiator. The mixture of polymers and initiator was degassed with Ar gas for 4 min, followed by sealing with Teflon tape. Polymerization was conducted at 70 °C for 24 h under vigorous stirring. After polymerization, a 10% concentration of product polymers was obtained, cooled to 25 °C, and stored at 4 °C before use. These ferrocene polymers (FcPs) were named FcP1, FcP2, FcP3, FcP4, and FcP5 based on the molar ratio of the polymers (FMMA = 0.4, MAA: PEGMA = 2:0, 1.5:0.5, 1:1, 0.5:1.5, and 0:2).

Characterization of FcPs: The chemical composition and purity of the polymers were characterized by proton nuclear magnetic resonance (^{1}H NMR) spectroscopy (400 MHz, 25 °C, Dimethyl sulfoxide-d_6 (DMSO d_6, 99.8%) (Merck, Darmstadt, Germany) as the deuterated solvent, JEOL JNM-ECZ400S/L1, Tokyo, Japan). Additionally, the weight average molecular weight (Mw; g mol^{-1}), number average molecular weight (Mn; g mol^{-1}), and polydispersity index (PDI, $Đ_M = Mw/Mn$) were measured via gel-permeation chromatography (GPC, Agilent 1200S/miniDAWN TREOS, Santa Clara, CA, USA) using relative calibration with polystyrene (PS) standards and THF as the eluent at a flow rate of 1.0 mL min^{-1} at 35 °C.

Fabrication and Characterization of the Ferrocene Nanoparticles (FcNPs): The CMC of the FcPs was measured using DLS (ZEN3600, Malvern Instruments, Malvern, UK), as previously described.[41] Aqueous solutions of FcPs were prepared in a concentration range from 5.05 × 10^{-8} to 4.04 × 10^{-6} mol L^{-1}. Measurements were conducted in a polystyrene cell at 25 °C. Detecting scattered light at a fixed angle of 173°, known as non-invasive backscatter, provided high sensitivity and signal quality, particularly when measuring the size of nanoparticles. FcNPs were fabricated using a nanoprecipitation method based on the self-assembly of amphiphilic FcPs composed of hydrophobic FMMA, hydrophilic MAA, and PEGMA polymers. First, 5 mg of FcPs diluted in 50 µL of THF (10% concentration) were mixed with 950 µL of THF at 25 °C. This FcP-containing solution was added dropwise to 5 mL of deionized water (DIW) (HyClone, Logan, UT, USA) using a syringe pump (LEGATO100, KD Scientific, Holliston, MA, USA) with magnetic stirring (530 rpm, 5 min). The FcNP-containing solution was then vacuum-dried for 2 h to stabilize the FcNPs by removing the THF solvent. The nanoparticles were named FcNPs (FcNP1s, FcNP2s, FcNP3s, FcNP4s, and FcNP5s) according to the FcP species used for fabrication. The hydrodynamic diameters and PDI of the FcNPs were analyzed using dynamic light scattering (DLS) (Zetasizer, ELSZ-2000 series; Otsuka Electronics Co., Ltd., Osaka, Japan). To assess the stability of the FcNPs, their hydrodynamic diameter and PDI were observed over time (1, 4, 7, 14, 21, and 42 days) in DIW, and their variations before lyophilization (3 days) and after redispersion were monitored using DLS analysis.

ROS-Sensitive Properties of the FcNPs: After monitoring the stability of the FcNPs, their ROS sensitivity was assessed over time. H_2O_2 (100 mM) 30% (w/w) (Junsei Chemical Co., Tokyo, Japan) was added to the FcNPs and kept them under 100 rpm at 37 °C. Variations in the hydrodynamic diameters and surface charges induced by the oxidative agent, H_2O_2, were observed at various time points using DLS analysis. The morphology of the FcNPs before and after the addition of the oxidative agent was examined using a transmission electron microscope (TEM, JEM-2100Plus HR; JEOL, Tokyo, Japan) operated at an acceleration voltage of 200 kV.

Characterization of Sulfasalazine-Loaded Ferrocene Nanoparticles (SSZ@FcNPs): SSZ (0, 0.25, 0.5, and 1 mg) was combined with 5 mg of FcPs diluted in 50 µL of THF (10% concentration) and subjected to rotary shaking at 25 °C for 2 h. The subsequent process for manufacturing SSZ@FcNPs was identical to that described in Section 2.3. The hydrodynamic diameter and PDI of SSZ@FcNPs were measured in DIW over time intervals of 1, 7, 14, 21, 42, and 84 days using DLS analysis. After confirming the stability of SSZ@FcNPs, the loading content (L.C.) and encapsulation efficiency (E.E.) of the drug-loaded FcNPs were measured by analyzing the amount of unloaded SSZ using high-performance liquid chromatography (HPLC, Waters 2695; Waters Corp., Milford, MA, USA). Unloaded SSZ was purified by ultrafiltration using Amicon Ultra-15 centrifugal filters (molecular weight cut-off (MWCO) 100 kDa) for 10 min at 1300 rpm. An RP-HPLC column (YMC – Triart C18, ø4.6 × 250 mm, 5 µm) was used to measure the quantity of unloaded SSZ in 20 µL of filtrate using a mixture of methanol-aqueous acetic acid solution (pH 5) with gradient elution mode for 12 min. Methanol, acetic acid, and water (all HPLC-grade) were purchased from Sigma-Aldrich. The HPLC conditions are listed in Table S1 (Supporting Information). The L.C. and E.E. of SSZ@FcNPs were calculated using the following equations:

$$\text{Loading contents (l.c., \%)} = \frac{\text{weight of SSZ} - \text{weight of unloaded SSZ}}{\text{weight of FcPs}} \times 100 \quad (1)$$

$$\text{Encapsulation efficiency (E.E, \%)} = \frac{\text{weight of SSZ} - \text{weight of unloaded SSZ}}{\text{weight of FcPs}} \times 100 \quad (2)$$

ROS-Sensitive Drug Release of SSZ@FcNPs: The ROS-sensitive properties of SSZ@FcNPs were analyzed over time. The hydrodynamic diameters of SSZ@FcNPs were measured at specific time points (0, 2, 4, 8, 18, 20, and 24 h) using DLS analysis. The samples were incubated in 1× PBS at pH 7.4 (HyClone, Logan, UT, USA) under conditions of 100 rpm and 37 °C, following treatment with 100 µM H_2O_2 as an oxidative agent.

The cumulative ROS-sensitive release of SSZ from SSZ@FcNPs was quantified using HPLC, as described in Section 2.5, by calculating the amount of SSZ released. Initially, SSZ@FcNPs were placed in a Float A-

Lyzer G2 dialysis device (MWCO = 100 kDa, Spectrapro/Pro dialysis membrane; Repligen, MAA, USA). The device was incubated under two conditions (PBS and PBS containing 100 µM H_2O_2) at 100 rpm and 37 °C. The release buffer was collected at various time points (2, 4, 8, 18, and 24 h).

The morphology of SSZ@FcNPs was examined before and after the addition of H_2O_2 using both photographic and TEM imaging. The TEM was operated at an accelerating voltage of 200 kV. For analysis, the copper grid was prepared by depositing 10 µL of SSZ@FcNPs and allowing it to air dry over three days.

Fabrication and Characterization of Enriched FcNPs and SSZ@FcNPs: To create a 4× enrichment of FcNPs, 20 mg of FcPs in 200 µL of THF (10% concentration) were combined with 800 µL of THF. Similarly, a 4× enrichment of SSZ@FcNPs was produced by mixing 20 mg of FcPs in 200 µL of THF (10% concentration) with 2 mg of SSZ in 800 µL of THF. For an 8× enrichment of FcNPs, 40 mg of FcPs in 400 µL of THF (10% concentration) were combined with 600 µL of THF. Likewise, an 8× enrichment of SSZ@FcNPs was created by mixing 40 mg of FcPs in 400 µL of THF (10% concentration) with 4 mg of SSZ in 600 µL of THF.

The fabrication process for enriched FcNPs and SSZ@FcNPs followed the method described in Section 2.3. To evaluate the stability of the enriched FcNPs and SSZ@FcNPs, they were placed in DIW at 25 °C and in PBS at 37 °C with 100 rpm. Their hydrodynamic diameters and PDI were monitored using DLS analysis. The morphology of the optimized enriched SSZ@FcNPs was examined using TEM at an accelerating voltage of 200 kV.

Isolation and Culture of Rheumatoid Patient Cells: Synovial fluid (SF) samples were collected from patients with rheumatoid arthritis (RA). Fibroblast-like synoviocyte cells were obtained following the protocols described in previous studies.[76,77] The synovial fluid was mixed with an equal volume of Hank's Balanced Salt Solution and centrifuged at 2500 rpm for 20 min. The resulting cell pellets were resuspended in 10 mL of MEMα supplemented with 10% fetal bovine serum (FBS) and 1% penicillin/streptomycin, then seeded into 100 mm cell culture dishes. Cultures were maintained at 37 °C in a humidified atmosphere containing 5% CO_2. Non-adherent cells were discarded, and adherent cells were cultured in MEMα with 10% FBS and 1% penicillin/streptomycin. The culture medium was refreshed every 2–3 days. Upon reaching over 90% confluence, the cells were harvested by trypsinization and passaged at a 1:5 ratio. Based on 15 mL of synovial fluid, 1–1.2 × 10^6 cells were obtained from a single 100 mm cell dish after 7 days of culture. The purity of SF-derived FLSs was confirmed using flow cytometry at passage 3. This study was approved by and conducted in compliance with the guidelines of the Gyeongsang National University Hospital Institutional Review Board (IRB) (Approval No. 2019-10-021).

Fabrication Method of PCL-Micropatterned Nanofibrous Microwells: Polycaprolactone (PCL)-micropatterned nanofibrous microwells were integrated into hydrogel micropatterns using photolithography, following previously established procedures.[78] Initially, PCL fibers were produced via electrospinning. A solution of 20 wt.% PCL (Molecular Weight: 80 000 g mol^{-1}, Sigma Aldrich) in 2,2,2-trifluoroethanol, containing 2-hydroxy-2-methylpropiophenone (HOMPP) as a photoinitiator (2% v/v), was extruded from a syringe pump through an 18G metal needle under a positive voltage of 7.5 kV, at a flow rate of 0.8 mL h^{-1} for 1 h.

Subsequently, 200 µL of precursor solution was applied onto the electrospun fibers. A photomask with square microarray patterns was placed over the scaffold and exposed to UV light (365 nm, EFOS Ultracure 100 ss Plus, UV spot lamp, Mississauga, ON, Canada) for 1 s to crosslink the hydrogels. After crosslinking, the unreacted precursor solution was rinsed off with water.

For cell studies, the scaffolds were sterilized in 70% (v/v) ethanol solution for 10 min, followed by two washes with PBS to remove residual ethanol.

In Vitro Immune Response Test Using Macrophages: RAW264.7 cells were seeded in a 24-well plate. Upon reaching 80% confluence, cells were treated with LPS, phosphate-buffered saline (PBS), FcNPs, or SSZ@FcNPs. After 24 h of incubation, immunofluorescence staining and western blotting were performed to evaluate the immune response.

Immunofluorescence Staining: Protein expression markers in 3D-cultured spheroids and patient tissues were assessed using immunofluorescence staining. The 3D spheroids and patient tissues were fixed with 4% paraformaldehyde (Dana, Korea) for 1 hour and permeabilized with Triton-X 100 at 23 °C for 2 h. Staining was conducted with primary antibodies overnight at 4 °C, followed by secondary antibodies and DAPI for 15 min at 23 °C. Actin filaments were additionally stained with phalloidin-iFluor 488 (1:400 dilution, catalog number ab176753, Abcam).

The primary antibodies used were CD68 (1:500 dilution, catalog number ab213363, Abcam, UK), CD86 (1:250 dilution, catalog number B273396, BioLegend, USA), and α-sma (1:500 dilution, catalog number ab5694, Abcam, UK). Following incubation with primary antibodies, the membranes were incubated with secondary antibodies: Goat Anti-Rabbit IgG H&L (Alexa Fluor 488) (1:1000 dilution, catalog number ab150077, Abcam, UK) and Goat Anti-Mouse IgG H&L (Alexa Fluor 647) (1:1000 dilution, catalog number ab150115, Abcam, UK).

Real-Time Quantitative Polymerase Chain Reaction (RT-qPCR): Gene expression levels were quantified using real-time quantitative polymerase chain reaction (RT-qPCR) on a Thermo Fisher QuantStudio 5 system (Applied Biosystems, USA). Cellular ribonucleic acid (RNA) was initially extracted using the TRIzol reagent, followed by purification with chloroform, isopropyl alcohol, and ethanol. RNA concentration was determined using a NanoDrop spectrophotometer. Complementary DNA (cDNA) synthesis was performed using the SuperScript VILO Master Mix (Invitrogen, USA) with 1 µg of RNA. The cDNA synthesis process involved incubation at 42 °C for 99 min, followed by termination at 85 °C for 5 min. The synthesized cDNA was stored at −80 °C until further use. For the qPCR analysis, an initial denaturation step was carried out at 95 °C for 10 min. Quantitative PCR was performed using target-specific primers and the QuantiNova SYBR Green PCR Kit (Qiagen, Netherlands).

Western Blot Assay: Proteins were extracted and lysed using the Cel-Lytic lysis reagent (Sigma-Aldrich) for western blot analysis. Samples containing 20 µg of protein were loaded onto a 10% SDS-PAGE gel and electrophoresed at 60 V for 20 min followed by 120 V for 60 min to separate the proteins. Separated proteins were then transferred onto a polyvinylidene difluoride (PVDF) membrane (Millipore, Billerica, MA, USA) using the wet transfer method with a Mini Trans–Blot module (Bio-Rad) at 300 mA for 90 min.

After transfer, the PVDF membrane was blocked with 5% nonfat dry milk in Tris-buffered saline containing 0.1% Tween-20 (TBS-T) for 1 h at 23 °C. Subsequently, the membrane was incubated overnight at 4 °C with primary antibodies diluted in TBS-T containing 5% bovine serum albumin (BSA). The primary antibodies used were: Anti-IKB alpha (phospho S36) antibody (1:10 000 dilution, catalog number ab133462, Abcam, UK), Anti-IκB alpha antibody (1:1000 dilution, catalog number ab32518, Abcam, UK), Anti-NF-κB p65 (phospho S536) antibody (1:1000 dilution, catalog number ab76302, Abcam, UK), Anti-NF-κB p65 antibody (1:1000 dilution, catalog number ab32536, Abcam, UK), Anti-NFκB p105/p50 antibody (1:1000 dilution, catalog number ab32360, Abcam, UK).

Following primary antibody incubation, the membrane was washed three times with TBS-T and then incubated with horseradish peroxidase (HRP)-conjugated secondary antibodies (1:8000, Cell Signaling Technology) for 1 h at 23 °C. Protein bands were visualized using ECL Select Western Blotting Detection Reagent (Cytiva) and imaged using an LAS4000 mini imaging system (Fujifilm Corp.).

Lactate Dehydrogenase (LDH) Assay: FLSs within a co-cultured 3D spheroid system on a 3D micro-patterned scaffold with HUVECs were analyzed for lactate dehydrogenase (LDH) release following drug treatment using an LDH Assay Kit (Dogenbio, Korea). A 10 µL sample of cell supernatant was collected and combined with 100 µL of water-soluble tetrazolium salt substrate mix. The mixture was incubated for 1 h at 37 °C in a 5% CO_2 atmosphere. Absorbance was measured at 450 nm using a microplate reader (Synergy H1, BioTek, VT, USA).

ROS Quantitative Assay (DCFDA/H2DCFDA Assay): ROS levels in FLSs within a co-cultured 3D spheroid system on a micro-patterned scaffold with HUVECs were measured following treatment with FcNPs and

SSZ@FcNPs using a DCFDA/H2DCFDA ROS assay (Abcam, UK). The cells were washed twice with DPBS and incubated with DCFDA solution for 1 h. The fluorescence intensity was measured at excitation/emission wavelengths of 485/535 nm using a microplate reader (Synergy H1, BioTek, VT, USA).

Fibroblast-Like Synoviocytes (FLS) Activation: To simulate the inflammatory environment and activate cells derived from patients with rheumatoid arthritis (RA), 1×10^5 cells were cultured on a 3D patterned scaffold for 4 days. Subsequently, cells were incubated with 10 ng mL^{-1} TNF-α (R&D Systems, USA) at 37 °C and 5% CO_2 for two days.

Drug Treatment on 3D Spheroid In Vitro Model: After co-culturing fibroblast-like synoviocytes (FLSs) derived from rheumatoid arthritis (RA) patients with HUVECs for 4 days, the cells were treated with 10 ng mL^{-1} TNF-α for 2 days to induce activation. Subsequently, the cells were treated with SSZ, FcNPs, and SSZ@FcNPs for an additional 2 days. Following treatments, subsequent assays were performed.

Dot Blot Assay Using Human Inflammatory Cytokine Array: The human inflammatory cytokine array (catalog number ab134003, Abcam, UK) was employed to detect multiple inflammatory cytokines released from fibroblast-like synoviocytes (FLSs). Initially, FLSs and HUVECs were co-cultured in a 3D environment for 4 days, followed by treatment with 10 ng mL^{-1} TNF-α for 2 days. Supernatants from both the treated and untreated groups were centrifuged to remove debris. The human inflammatory cytokine array was then blocked with blocking solution for 30 min at 23 °C, followed by incubation with centrifuged supernatants for 2 h at 23 °C. After washing with wash buffer, biotin-conjugated anti-cytokines and HRP-conjugated streptavidin were sequentially applied and incubated overnight at 4 °C. Chemiluminescence signals were detected using an LAS-4000 imaging system (Fujifilm Life Science, USA).

Animals and Arthritis Induction: Six-week-old male DBA/1J mice were purchased from the Central Lab. Animal, Inc. (Seoul, Korea). All experimental procedures were conducted in accordance with the guidelines of Gyeongsang National University (GNU) and approved by the Institutional Animal Care and Use Committee (IACUC approval ID: GNU-240527-M0108) of Korea. CIA was induced as described previously.[79,80] Briefly, DBA/1 mice were intradermally immunized with bovine type II collagen (CII; Chondrex, Redmond, WA, USA) emulsified in complete Freund's adjuvant (CFA; Sigma-Aldrich) on day 0. Immunization was boosted with an equal volume of CII-emulsified incomplete Freund's adjuvant (IFA; Chondrex) on day 21. Beginning on day 1, mice were treated twice weekly via intra-orbital sinus injection with PBS, Sulfasalazine (SSZ, 0.4 mg ml^{-1}), Ferrocene nanoparticles (FcNPs, 0.4 mg ml^{-1}), or SSZ-loaded ferrocene nanoparticles (SSZ@FcNPs, 0.4 mg ml^{-1}).

Arthritis Scoring: Clinical arthritis scores were assessed on a scale ranging from 0 to 4, representing the sum of the scores for each limb. The scores were assigned as follows: 0 for no swelling, 1 for slight swelling and erythema, 2 for moderate swelling and erythema, 3 for severe swelling and erythema, and 4 for maximal inflammation with joint rigidity. The maximum possible score per mouse was 16.

Flow Cytometric Analysis: As described previously, immune cell extraction and stimulation were conducted in the inguinal lymph nodes.[81] That is, immune cells were extracted from inguinal lymph nodes via mechanical grinding and prepared as single-cell suspensions. The isolated cells were stimulated with 50 ng ml^{-1} PMA (phorbol 12-myristate 13-acetate, Sigma-Aldrich, MA, USA) and 500 ng ml^{-1} ionomycin (Sigma-Aldrich) in the presence of a protein transport inhibitor (BD GolgiPlug, BD Biosciences, NJ, USA) for 4 h at 37 °C. After stimulation, the cells were harvested and stained with a fixable viability dye (Thermo Fisher Scientific) and fluorochrome-conjugated antibodies against CD4. Following surface antigen staining, cells were fixed, permeabilized, and stained with fluorescein-labeled antibodies (all from eBioscience) against IFN-γ and IL-17A for 30 min at 23 °C. The stained cells were analyzed using a BD LSR Fortessa X-20 flow cytometer (BD Biosciences, NJ, USA).

Enzyme-Linked Immunosorbent Assay (ELISA): Cytokine detection in the culture supernatant was performed using sandwich ELISA as previously described.[82] Briefly, to quantify IFN-γ and IL-17A levels in inguinal lymph node cell culture supernatants, 96-well plates (Greiner Bio-One GmbH, Frickenhausen, Germany) were coated with monoclonal antibodies against IFN-γ (eBioscience, San Diego, CA, USA) or IL-17A (eBioscience) and blocked with BD OptEIA Assay diluent (BD Biosciences). Samples were added to the wells and incubated overnight at 4 °C. Biotinylated antibodies against IFN-γ (eBioscience) or IL-17A (eBioscience) were added, followed by AKP-conjugated streptavidin (BD Biosciences). Color development was achieved by adding a 5 mM phosphatase substrate (Sigma-Aldrich), and the absorbance was measured at 405 nm using a VersaMax microplate reader (Molecular Devices, Wokingham, UK) with SoftMax Pro 6.5.1 software.

Histological Examination: The ankle joint tissues were fixed in 10% formalin, decalcified for 4 weeks in 10% EDTA, and subsequently embedded in paraffin. Sections of 5 µm thickness were prepared and stained with hematoxylin and eosin (H&E) or safranin O. Evaluation of synovial inflammation, cartilage damage, and bone erosion were conducted as previously described.[83]

Serum Test: Following treatment with SSZ, FcNPs, and SSZ@FcNPs in vivo, the serum levels of urea and creatinine were quantitatively measured using colorimetric assay kits (Elabscience, USA). For creatinine measurement, 12 µL of serum was mixed with 180 µL of enzyme solution A and incubated at 37 °C for 5 min. Solution B was then added, and absorbance was measured at 515 nm using a microplate reader (Synergy H1, BioTek, VT). For urea measurement, 10 µL of serum was mixed with 125 µL of enzyme solution and incubated at 37 °C for 10 min. Subsequently, 1 mL of chromogenic agent and alkaline NaClO mix were added, followed by incubation at 37 °C for 10 min. Absorbance was measured at 580 nm using a microplate reader.

Statistical Methods: Each experiment was performed in triplicate ($n = 3$). Results were presented as mean ± standard deviation. Statistical differences between groups were assessed using Student's *t*-test and one-way analysis of variance (ANOVA). Statistical significance was defined as $*p < 0.05$; $**p < 0.01$; $***p < 0.001$; $****p < 0.0001$.

Supporting Information

Supporting Information is available from the Wiley Online Library or from the author.

Acknowledgements

D.K., C.K., and S.E.L. contributed equally to this work. This work was supported by a National Research Foundation of Korea (NRF) grant funded by the Korean Government (MSIT) (2021M3C1C3097647, 2021R1A2C2014268). This study was supported by a grant from the Korea Institute of Ceramic Engineering and Technology (KICET) (2410002182). This research was supported by the National Research Foundation of Korea (NRF), funded by the MSIT (No. RS-2023-00219399). This research was supported by grants from the Ministry of Trade, Industry, and Energy, Republic of Korea (No. 20018522) and the Korea Health Technology R&D Project through the Korea Health Industry Development Institute (KHIDI), funded by the Ministry of Health and Welfare, Republic of Korea (No. HI22C1394). All completed graphics in this manuscript were created using BioRender and are accompanied by the following citation: "Created in BioRender. Afbl, S. (2024) BioRender.com/q52z539." We would like to thank Editage (www.editage.co.kr) for English language editing.

Conflict of Interest

The authors declare no conflict of interest.

Data Availability Statement

The data that support the findings of this study are available in the supplementary material of this article.

Keywords

3D hyperplasia model, ferrocenes, reactive oxygen species (ROS), rheumatoid arthritis, sulfasalazine

Received: September 1, 2024
Revised: December 3, 2024
Published online:

[1] J. Bullock, S. A. A. Rizvi, A. M. Saleh, S. S. Ahmed, D. P. Do, R. A. Ansari, J. Ahmed, *Med. Princ. Pract.* **2018**, *27*, 501.
[2] H. U. Scherer, T. Häupl, G. R. Burmester, *J. Autoimmun.* **2020**, *110*, 102400.
[3] E. Mysler, M. Caubet, A. Lizarraga, *Open Access Rheumatol.: Res. Rev.* **2021**, *13*, 139.
[4] H. Cooley, T. Smith, P. Youssef, K. Tymms, D. Mathers, S. Ciciriello, H. Griffiths, C. OSullivan, G. Littlejohn, *Arthritis Rheumatol.* **2020**, *72*, 12.
[5] Z. Ozsoy, A. Ozdemir, M. Ekici, E. Bilgin, L. Kilic, S. Kiraz, Z. Saribas, B. Sener, O. Karadag, *Rheumatol. Int.* **2023**, *43*, 1445.
[6] M. Lora, H. A. Menard, *J. Rheumatol.* **2007**, *34*, 1615
[7] B. Bartok, G. S. Firestein, *Immunol. Rev.* **2010**, *233*, 233.
[8] H. Yoshitomi, *Front. Immunol.* **2019**, *10*, 1395.
[9] M. F. Bustamante, R. Garcia-Carbonell, K. D. Whisenant, M. Guma, *Arthritis Res. Ther.* **2017**, *19*, 110.
[10] L. N. Samimi, E. Farhadi, M. N. Tahmasebi, A. Jamshidi, A. S. Vaziri, M. Mahmoudi, *Autoimmun. Highlights* **2020**, *11*, 1110
[11] B. Y. Kang, S. W. Chung, S. Y. Im, Y. K. Choe, T. S. Kim, *Immunology* **1999**, *98*, 98.
[12] S. M. Rad, N. Abdolahi, A. Soltani, *Ann. Rheum. Dis.* **2019**, *78*, 1657.
[13] M. Shadid, G. Gurau, J. L. Shamshina, B. C. Chuang, S. Hailu, E. Guan, S. K. Chowdhury, J. T. Wu, S. A. A. Rizvi, R. J. Griffin, R. D. Rogers, *MedChemComm* **2015**, *6*, 1837.
[14] A. Priyam, K. Shivhare, S. Yadav, A. K. Sharma, P. Kumar, *Colloids Surf., A* **2018**, *547*, 157.
[15] M. L. Jelicic, E. Brusac, S. Kurajica, M. Cvetnic, D. A. Klaric, B. Nigovic, A. Mornar, *Pharmaceutics* **2021**, *13*, 400.
[16] S. Dolati, S. Sadreddini, D. Rostamzadeh, M. Ahmadi, F. Jadidi-Niaragh, M. Yousefi, *Biomed. Pharmacother.* **2016**, *80*, 30.
[17] A. Sharma, A. Goel, *Nano Life* **2023**, *13*, 23300066.
[18] Y. Na, J. S. Lee, J. Woo, S. Ahn, E. Lee, W. I. Choi, D. Sung, *J. Mater. Chem. B* **2020**, *8*, 1906.
[19] V. Previtali, N. Woodworth, M. H. Hopkins, J. H. Petersen, I. Ahnfelt-Ronne, M. H. Clausen, *Ann. Rheum. Dis.* **2019**, *78*, A62.
[20] B. Chance, H. Sies, A. Boveris, *Physiol. Rev.* **1979**, *59*, 527.
[21] R. Pietschnig, *Chem. Soc. Rev.* **2016**, *45*, 5216.
[22] F. Xu, H. Li, Y.-L. Luo, W. Tang, *ACS Appl. Mater. Interfaces* **2017**, *9*, 5181.
[23] M. Aghaei, V. Erfani-Moghadam, L. Daneshmandi, A. Soltani, N. Abdolahi, M. Cordani, A. Yahyazadeh, S. M. Rad, S. Tavassoli, H. Balakheyli, *J. Mol. Struct.* **2021**, *1230*, 129874.
[24] C. Kinnear, H. Dietsch, M. J. Clift, C. Endes, B. Rothen-Rutishauser, A. Petri-Fink, *Angew. Chem.* **2013**, *125*, 1988.
[25] H. Ye, Y. Zhou, X. Liu, Y. Chen, S. Duan, R. Zhu, Y. Liu, L. Yin, *Biomacromolecules* **2019**, *20*, 2441.
[26] F. Seidi, R. Jenjob, D. Crespy, *Chem. Rev.* **2018**, *118*, 3965.
[27] Y. Wang, R. Guo, M. Zou, L. Jiang, L. Kong, S. Zhao, X. Zhang, W. Wang, B. Xu, *Int. J. Nanomed.* **2024**, *19*, 4217.
[28] P. Conigliaro, P. Triggianese, E. De Martino, G. L. Fonti, M. S. Chimenti, F. Sunzini, A. Viola, C. Canofari, R. Perricone, *Autoimmun. Rev.* **2019**, *18*, 706.
[29] S. Suissa, N. Baker, A. Ravindran, H. Kawabata, T. Simon, *Ann. Rheum. Dis.* **2015**, *74*, 328
[30] D. Kim, J. Heo, B. Song, G. Y. B. Lee, C. G. Hong, Z. M. Jiang, S. H. Lee, K. W. Lee, M. Kim, M. H. Park, *Mater. Today Bio* **2024**, *26*, 101061.
[31] Y. Y. Khine, Y. Jiang, A. Dag, H. Lu, M. H. Stenzel, *Macromol. Biosci.* **2015**, *15*, 1091.
[32] H. Oh, E. Jeong, J. S. Lee, J. Kim, D. Lee, B. S. Kim, D. Sung, H. Koo, W. I. Choi, G. Tae, *Mater. Today Bio* **2023**, *22*, 100774.
[33] R. Gracia, D. Mecerreyes, *Polym. Chem.* **2013**, *4*, 2206.
[34] X. Zhang, K. Takegoshi, K. Hikichi, *Polym. J.* **1991**, *23*, 79.
[35] A. Cesari, M. A. Casulli, T. Hashimoto, T. Hayashita, *Int. J. Mol. Sci.* **2022**, *23*, 6045.
[36] H. Zhang, X. Ma, C. Lin, B. Zhu, *RSC Adv.* **2014**, *4*, 33713.
[37] J. Kim, K. J. Baek, S. Yu, H. S. Yang, N. U. Khaliq, W. I. Choi, H. Kim, D. Sung, *Electrochim. Acta* **2023**, *463*, 142824.
[38] A. Kubotera, R. Saito, *Polym. J.* **2016**, *48*, 611.
[39] K. Li, Y. Cao, *Soft Mater.* **2010**, *8*, 226.
[40] S. Lee, Y. Na, K. H. Seol, W. I. Choi, D. Sung, J. Chang, *J. Electrochem. Soc.* **2020**, *167*, 136515.
[41] A. Gupta, A. P. Costa, X. M. Xu, S. L. Lee, C. N. Cruz, Q. Y. Bao, D. J. Burgess, *Int. J. Pharm.* **2020**, *583*, 119340.
[42] U. B. Hadkar, A. S. Hadkar, *Indian J. Pharm. Educ. Res.* **2015**, *49*, 134.
[43] C. Fornaguera, C. Solans, *Pharm. Nanotechnol.* **2018**, *6*, 147.
[44] I. Emaldi, S. Hamzehlou, J. Sanchez-Dolado, J. R. Leiza, *Processes* **2017**, *5*, 19.
[45] M. Ding, Z. Qian, J. Wang, J. Li, H. Tan, Q. Gu, Q. Fu, *Polym. Chem.* **2011**, *2*, 885.
[46] W. Abdelwahed, G. Degobert, S. Stainmesse, H. Fessi, *Adv. Drug Delivery Rev.* **2006**, *58*, 1688.
[47] S. R. Mane, I. L. Hsiao, M. Takamiya, D. Le, U. Straehle, C. Barner-Kowollik, C. Weiss, G. Delaittre, *Small* **2018**, *14*, 1801571.
[48] H. Otsuka, Y. Nagasaki, K. Kataoka, *Adv. Drug Delivery Rev.* **2003**, *55*, 403.
[49] L. Liu, L. Rui, Y. Gao, W. Zhang, *Polym. Chem.* **2015**, *6*, 1817.
[50] S. Lin, H. Zhao, C. Xu, P. Zhang, X. Mei, D. Jiang, *Mater. Des.* **2023**, *225*, 111465.
[51] Y. Zhao, S. Song, D. Wang, H. Liu, J. Zhang, Z. Li, J. Wang, X. Ren, Y. Zhao, *Nat. Commun.* **2022**, *13*, 6758.
[52] R. H. Staff, M. Gallei, M. Mazurowski, M. Rehahn, R. d. Berger, K. Landfester, D. Crespy, *ACS Nano* **2012**, *6*, 9042.
[53] Y. Xu, L. Wang, Y.-K. Li, C.-Q. Wang, *Carbohydr. Polym.* **2014**, *114*, 27.
[54] X. Zhu, Q. Chen, L. Xie, W. Chen, Y. Jiang, E. Song, Y. Song, *Acta Biomater.* **2022**, *145*, 210.
[55] M. Zhang, S. Hu, J. Tao, W. Zhou, R. Wang, Y. Tai, F. Xiao, Q. Wang, W. Wei, *Inflammopharmacology* **2019**, *27*, 845.
[56] I. M. Oliveira, D. C. Fernandes, I. F. Cengiz, R. L. Reis, J. M. Oliveira, *J. Mater. Sci.:Mater. Med.* **2021**, *32*, 74.
[57] J. A. Badillo-Mata, T. A. Camacho-Villegas, P. H. Lugo-Fabres, *Cells* **2022**, *11*, 3410.
[58] A. E. Koch, P. J. Polverini, S. J. Leibovich, *Arthritis Rheumatol.* **1986**, *29*, 471.
[59] N. Sofat, R. Wait, S. D. Robertson, D. L. Baines, E. H. Baker, *Front. Microbiol.* **2015**, *5*, 783.
[60] M. K. Demoruelle, K. D. Deane, V. M. Holers, *Curr. Opin. Rheumatol.* **2014**, *26*, 64.
[61] S. A. Agere, N. Akhtar, J. M. Watson, S. Ahmed, *Front. Immunol.* **2017**, *8*, 1341.
[62] S. Blüml, C. Scheinecker, J. S. Smolen, K. Redlich, *Int. Immunol.* **2012**, *24*, 275.
[63] H. Y. Song, M. Y. Kim, K. H. Kim, I. H. Lee, S. H. Shin, J. S. Lee, J. H. Kim, *Exp. Mol. Med.* **2010**, *42*, 565.
[64] C. Wahl, R. M. Schmid, G. Adler, S. Liptay, *Gastroenterology* **1998**, *114*, A1112.

[65] J. A. Roman-Blas, S. A. Jimenez, *Osteoarthritis Cartilage* **2006**, *14*, 839.
[66] N. Kondo, T. Kanai, M. Okada, *Curr. Issues Mol. Biol.* **2023**, *45*, 3000.
[67] Y. Y. Wu, C. C. Chen, C. C. Chyau, S. Y. Chung, Y. W. Liu, *Acta Pharmacol. Sin.* **2007**, *28*, 258.
[68] C. Atri, F. Z. Guerfali, D. Laouini, *Int. J. Mol. Sci.* **2018**, *19*, 1801.
[69] G. Lopez-Castejon, D. Brough, *Cytokine Growth Factor Rev.* **2011**, *22*, 189.
[70] S. Liptay, M. Bachem, G. Häcker, G. Adler, K. M. Debatin, R. M. Schmid, *Brit. J. Pharmacol.* **1999**, *128*, 1361.
[71] V. Tugcu, E. Ozbek, A. I. Tasci, E. Kemahli, A. Somay, M. Bas, C. Karaca, T. Altug, M. B. Çekmen, H. K. Özdogan, *BJU Int.* **2006**, *98*, 680.
[72] M. Chabaud, J. M. Durand, N. Buchs, F. Fossiez, G. Page, L. Frappart, P. Miossec, *Arthritis Rheumatol.* **1999**, *42*, 963.
[73] M. Chabaud, P. Garnero, J. M. Dayer, P. A. Guerne, F. Fossiez, P. Miossec, *Cytokine* **2000**, *12*, 1092.
[74] M. Kim, Y. H. Choe, S. I. Lee, *Immune Netw.* **2022**, *22*, e8.
[75] M. I. Koenders, E. Lubberts, B. Oppers-Walgreen, L. van den Bersselaar, M. M. Helsen, J. K. Kolls, L. A. B. Joosten, W. B. van den Berg, *Arthritis Rheumatol.* **2005**, *52*, 975.
[76] J. A. Stebulis, R. G. Rossetti, F. J. Atez, R. B. Zurier, *J. Rheumatol.* **2005**, *32*, 301.
[77] J. H. Jung, J. S. Lee, Y. G. Kim, C. K. Lee, B. Yoo, E. C. Shin, S. K. Hong, *Clin. Transl. Immunol.* **2020**, *9*, e1140.
[78] H. S. Shin, Y. M. Kook, H. J. Hong, Y. M. Kim, W. G. Koh, J. Y. Lim, *Acta Biomater.* **2016**, *45*, 121.
[79] M. Kim, Y. Choe, H. Lee, M. G. Jeon, J. H. Park, H. S. Noh, Y. H. Cheon, H. J. Park, J. Park, S. J. Shin, K. Lee, S. I. Lee, *Exp. Mol. Med.* **2021**, *53*, 67.
[80] D. D. Brand, K. A. Latham, E. F. Rosloniec, *Nat. Protoc.* **2007**, *2*, 1269.
[81] S. Kim, S. H. Chun, S. T. Hong, Y. H. Cheon, M. Kim, H. Lee, H. O. Kim, S. I. Lee, Y. S. Suh, *Ann. Rheum. Dis.* **2023**, *82*, 136.
[82] D. Kim, M. Kim, T. W. Kim, Y. H. Choe, H. S. Noh, H. M. Jeon, H. Kim, Y. E. Lee, G. Hur, K. M. Lee, K. Shin, S. I. Lee, S. H. Lee, *J. Exp. Med.* **2022**, *219*, 20200795.
[83] S. Hayer, M. J. Vervoordeldonk, M. C. Denis, M. Armaka, M. Hoffmann, J. Bäcklund, K. S. Nandakumar, B. Niederreiter, C. Geka, A. Fischer, N. Woodworth, S. Blüml, G. Kollias, R. Holmdahl, F. Apparailly, M. I. Koenders, *Ann. Rheum. Dis.* **2021**, *80*, 714.